Laser Raman spectroscopy as a technique for identification of seafloor hydrothermal and cold seep minerals

Sheri N. White *

Department of Applied Ocean Physics and Engineering, Woods Hole Oceanographic Institution, Woods Hole, MA 02536, USA

ARTICLE INFO

ABSTRACT

In situ sensors capable of real-time measurements and analyses in the deep ocean are necessary to fulfill the potential created by the development of autonomous, deep-sea platforms such as autonomous and remotely operated vehicles, and cabled observatories. Laser Raman spectroscopy (a type of vibrational spectroscopy) is an optical technique that is capable of in situ molecular identification of minerals in the deep ocean. The goals of this work are to determine the characteristic spectral bands and relative Raman scattering strength of hydrothermally- and cold seep-relevant minerals, and to determine how the quality of the spectra are affected by changes in excitation wavelength and sampling optics. The information learned from this work will lead to the development of new, smaller sea-going Raman instruments that are optimized to analyze minerals in the deep ocean.

Many minerals of interest at seafloor hydrothermal and cold seep sites are Raman active, such as elemental sulfur, carbonates, sulfates and sulfides. Elemental S_8 sulfur is a strong Raman scatterer with dominant bands at ~219 and 472 Δcm^{-1}. The Raman spectra of carbonates (such as the polymorphs calcite and aragonite) are dominated by vibrations within the carbonate ion with a primary band at ~1085 Δcm^{-1}. The positions of minor Raman bands differentiate these polymorphs. Likewise, the Raman spectra of sulfates (such as anhydrite, gypsum and barite) are dominated by the vibration of the sulfate ion with a primary band around 1000 Δcm^{-1} (~1017 for anhydrite, ~1008 for gypsum, and ~988 for barite). Sulfides (pyrite, marcasite, chalcopyrite, isocubanite, sphalerite, and wurtzite) are weaker Raman scatters than carbonate and sulfate minerals. They have distinctive Raman bands in the ~300–500 Δcm^{-1} region. Raman spectra from these mineral species are very consistent in band position and normalized band intensity. High quality Raman spectra are obtained from all of these minerals using both green and red excitation lasers, and using a variety of sampling optics. The highest quality spectra (highest signal-to-noise) were obtained using green excitation (532 nm Nd:YAG laser) and a sampling optic with a short depth of focus (and thus high power density). Significant fluorescence was not observed for the minerals analyzed using green excitation.

Spectra were also collected from pieces of active and inactive hydrothermal chimneys, recovered from the Kilo Moana vent field in 2005 and 11°N on the East Pacific Rise in 1988, respectively. Profiles of sample J2-137-1-r1-a show the transition from the chalcopyrite-rich "inner" wall to the sphalerite-dominated "outer" wall, and indicate the presence of minor amounts of anhydrite. Spectra collected from sample A2003-7-1a5 identify Cu–S tarnishes present on the surface of the sample.

1. Introduction

The future of oceanography is being shaped by the development of new underwater platforms that are autonomously or remotely operated. These include remotely operated vehicles (ROVs), autonomous underwater vehicles (AUVs), deep-sea moorings and seafloor cabled observatories. These platforms are most efficient when equipped with instruments capable of in situ measurements and analyses. That is, they are changing oceanography from a "sampling" science to a "sensing" science. Some oceanographic disciplines are already well suited to this new paradigm. The primary instrument of the physical oceanographer is the CTD (Conductivity–Temperature–Depth sensor), and marine geophysicists routinely deploy magnetometers, gravimeters, and seafloor seismometers. However, the disciplines of chemistry, biology and geology are lagging in in situ technology (Varney, 2000; Daly et al., 2004; Prien, 2007). Technologies are now becoming available that can identify the chemical composition of minerals in situ in the deep ocean.

1.1. Hydrothermal vents and cold seeps

One area in particular that would benefit from new sensing technology is the study of seafloor hydrothermal and cold seep systems. Hydrothermal vents occur along seafloor spreading ridges throughout

* Woods Hole Oceanographic Institution, Blake 209, MS#7, Woods Hole, MA 02543, USA. Tel.: +1 508 289 3740; fax: +1 508 457 2006.
    E-mail address: swhite@whoi.edu.

the world ocean (Baker and German, 2004). Cold seawater circulates within recently formed, still hot crust, above a magma lens, where it is heated and reacts with the host rock. Modification of the fluid includes removal of Mg, exchange of Ca for Na, and addition of metals and volatiles (Alt, 1995). The modified fluid rises buoyantly to the surface where it exits the seafloor as focused, high-temperature (~350 °C) vents or lower-temperature (~20 °C) diffuse flow. At highest-temperature vents, the hydrothermal fluid mixes with seawater above the vent orifice, resulting in precipitation of metal-bearing phases in the rising plume — thus receiving the name "black smokers." Anhydrite- and sulfide-rich chimneys are formed at vent orifices, and they evolve and mature (Goldfarb et al., 1983; Haymon, 1983). Hydrothermal fluids and mineral deposits exhibit compositional ranges, based in part on the host rock (e.g., basalt, enriched mid-ocean ridge basalt, andesite, rhyolite, peridotite, presence or absence of sediment), and in part on styles of mixing (e.g., Tivey, 1995; Hannington et al., 2005; Tivey, 2007). Hydrothermal vent fields are also home to unique biological communities that are supported by chemosynthetic bacteria and archaea (Hessler and Kaharl, 1995). Studying the variety of minerals that are deposited and precipitated at hydrothermal vent sites can provide insights into those processes occurring in the subsurface that affect ocean chemistry and the seafloor biological communities.

Cold seeps are sites where natural gas (primarily methane) is percolating through the seafloor. These sites often occur along continental margins, such as Hydrate Ridge off the coast of Oregon, where in some cases, gas bubbles are actively venting from the sea floor. At the proper pressure and temperature conditions, the gas and water mix to form solid clathrate hydrates. Clathrate hydrate is an ice-like lattice that holds gas molecules (e.g., carbon dioxide, methane and higher hydrocarbons) in cages in the lattice structure. The gas-rich fluids at these seep sites support chemosynthetic communities similar to those at hydrothermal vents — bacterial mats, clams, mussels, tube worms, etc. (Sibuet and Olu, 1998). Carbonate crusts (which can include calcite and dolomite) are also known to form in cold seep regions (Aloisi et al., 2000, 2002; Luff et al., 2004).

1.2. Laser Raman spectroscopy in the ocean

Laser Raman spectroscopy (a type of vibrational spectroscopy) is an optical technique, well suited to extreme environments, that is capable of in situ molecular identification of solids, liquids, and gases. Raman spectroscopy is non-invasive, non-destructive and does not require reagents or consumables. A laser excites a target, and the spectrum of the energy-shifted, back-scattered radiation serves as a "fingerprint" — providing compositional and structural information. The Raman scattered photons can have lower or higher energies than the incident photons — Stokes and anti-Stokes scattering, respectively. In this paper we look only at the Stokes (lower energy, higher wavelength) scattering. The spectrum is plotted as intensity vs. Raman shift in wavenumbers (Δcm^{-1}), shifted from the absolute frequency (in cm^{-1}) of the excitation laser. A more detailed discussion of Raman theory can be found in Ferraro et al. (2003) and Nakamoto (1997), and references therein. Raman spectroscopy has been used successfully for mineral identification in the laboratory (e.g., Haskin et al., 1997; Pasteris, 1998; Nasdala et al., 2004) and is capable of distinguishing between mineral polymorphs (e.g., calcite and aragonite, which are both $CaCO_3$). Many rocks and minerals found in the deep ocean are Raman active. These include components of basalt, and hydrothermal minerals such as anhydrite, sphalerite, chalcopyrite, and others. Raman spectroscopy is also well suited to making measurements in the ocean because water is a relatively weak Raman scatterer (Williams and Collette, 2001).

A sea-going Raman instrument (DORISS — Deep Ocean Raman In Situ Spectrometer) has been developed and deployed at a variety of sites in the deep ocean (Brewer et al., 2004; Pasteris et al., 2004). This system was built as a proof-of-concept with a broad spectral range (100–4400 Δcm^{-1})

and thus is capable of analyzing a large variety of solids, liquids and gases. DORISS consists of a 532 nm Nd:YAG excitation laser and a laboratory-model spectrometer with a duplex holographic grating and a TE-cooled CCD camera. The green laser was chosen for its high transmission through water. A remote optical head, connected to the laser and spectrometer via fiber optic cables, is capable of using a stand-off optic behind a pressure window with a working distance of up to 15 cm or an immersion optic with a sapphire window and a 6 mm working distance (Brewer et al., 2004). DORISS has been used to identify and analyze gas mixtures (White et al., 2006a), gas hydrates (Hester et al., 2006, 2007), and minerals. Naturally occurring minerals identified in situ by Raman spectroscopy to date include hydrothermally produced barite and anhydrite, calcite and aragonite in shells, and bacterially produced sulfur (White et al., 2005, 2006b).

Although DORISS has been used successfully in the ocean, the instrumentation, technique and data analysis methods have not been fully explored and developed (optimized) for hydrothermal vent and cold seep applications. The current work builds on initial deployments of the DORISS instrument to identify seafloor minerals. The goals of this work are to determine the characteristic spectral bands and Raman scattering strength of hydrothermally- and cold seep-relevant minerals, and to determine how the quality of the spectra are affected by changes in excitation wavelength and sampling optics. The information learned from this work will lead to the development of new, smaller sea-going Raman instruments that are optimized to analyze minerals in the deep ocean.

2. Application of laser Raman spectroscopy to mineralogy

Raman spectroscopy has been applied to minerals (e.g., Landsberg and Mandelstam, 1928) since its discovery in 1928 (Raman and Krishnan, 1928). Recent reviews by Smith and Carabatos-Nédelec (2001) and Nasdala et al. (2004) provide thorough discussions of the application of Raman spectroscopy to minerals and crystals. It should be noted that the Raman spectra of crystals are not as consistent as the spectra of gases and liquids. That is, the band positions and relative band intensities may vary slightly from one spectrum to another due to the orientation of the crystal lattice (and optical properties of the crystal) and/or the presence of local impurities or irregularities in the crystal structure. Typically, in the literature, band positions are reported, but not band intensity. Band intensity may be suggested by identifying the primary bands, or by the indicators "w" (weak) "m" (moderate) "s" (strong), or "vs" (very strong). In this paper, normalized band intensities (i.e., the band height above background divided by the height of the dominant band) and the range of those intensities will be reported to show how much variation in intensity one may expect to observe.

Raman spectroscopy is well suited to qualitative species identification. However, for quantitative analyses, Raman band heights in raw spectra cannot be used to straightforwardly infer concentration or abundance. This is due to the fact that different species have different Raman scattering efficiencies. Additionally, for heterogeneous samples, the species abundance in the area of the of sample illuminated by the laser spot may not be characteristic of the entire sample. For well mixed samples, such as liquids and gases, ratio techniques can be used to obtain information on relative concentration (e.g., Wopenka and Pasteris, 1987). For solid species, point-counting techniques can be used to determine relative abundance of minerals in a sample (e.g., Haskin et al., 1997). There are a number of issues to take into consideration when using a such a point-counting technique in mineral samples. The spectra obtained at each point in a grid will be affected by the spot size relative to the mineral's grain size, grain orientation, transparency to the excitation wavelength, etc. These issues are covered in more detail in Haskin et al. (1997). The application of such a point-counting technique to filter samples of hydrothermal plume minerals is discussed in Breier et al. (submitted for publication).

Table 1
Mineral standards and natural samples used in study

Mineral	Formula	Source	Sample number
Sulfur	S_8	J. Huber, MBL	–
Calcite	$CaCO_3$	Fisher Scientific	Rock collection #6
Aragonite	$CaCO_3$	Seafloor shell from Hydrate Ridge	–
Anhydrite	$CaSO_4$	M. Tivey, WHOI	A2178-3-1-Anh
			J2-137-1-R1-A
Gypsum	$CaSO_4–2H_2O$	Fisher Scientific	–
Barite	$BaSO_4$	Fisher Scientific	–
Pyrite	FeS_2	M. Tivey, WHOI	A2178-3-1-Py
Marcasite	FeS_2	M. Tivey, WHOI	J2-135-5-R1-Mc
Chalcopyrite	$CuFeS_2$	M. Tivey, WHOI	A2003-7-1a5
			J2-137-1-R1-A
		Wards Natural Science	
Isocubanite	$CuFe_2S_3$	M. Tivey, WHOI	A2467 RO1 P14MC
Sphalerite	(Zn,Fe)S	Wards Natural Science	–
Wurtzite	(Zn,Fe)S	M. Tivey, WHOI	A2944-3-s1-w1

Two challenges of laser Raman spectroscopy for mineral identification are laser-induced sample alteration and fluorescence. Although laser Raman spectroscopy is a non-destructive technique, samples can undergo localized heating and oxidation if the laser power is too high (what is considered "high" laser power depends on the sample). In our lab, samples under laser illumination were monitored carefully to detect any changes in the sample or in the Raman spectrum over time. In the ocean, the thermal sink of ambient seawater is able to dissipate excess heating. Fluorescence is more intense and longer-lived than Raman scattering. Thus, with a continuous-wave laser, fluorescence can easily overwhelm the Raman scattering signal. This optical interference is particularly an issue with blue–green excitation, which can induce fluorescence in organic material. This problem is discussed further in Section 6.2.

3. Experimental

3.1. Materials

Mineral standards and natural samples were obtained from a variety of sources and are listed in Table 1. Samples of quartz, gypsum and barite, and an educational rock and mineral collection were purchased from Fisher Scientific. Samples of sphalerite and chalcopyrite were purchased from Ward's Natural Science in Rochester, NY. Naturally occurring samples of euhedral anhydrite and sulfide minerals recovered from seafloor hydrothermal vent fields were provided by M. K. Tivey (WHOI). These samples were collected using DSV *Alvin* and ROV *Jason*. Pure mineral grains, identified based on crystal morphology and color, were hand picked from bulk rock samples under a Leica stereomicroscope. In

the case of isocubanite, the mineral was analyzed in an epoxy-impregnated polished thin section. Mineral identification of the thin section was made with a petrographic microscope (Leitz Laborlux 12 POL S) using reflected light. A sample of elemental sulfur was provided by J. Huber (Marine Biological Lab). This material was obtained on the Submarine Ring of Fire 2006 cruise to the Mariana Arc where, during a dive to a volcano site, the ROV *Jason II* was coated with molten sulfur from an active eruption (Nakamura et al., 2006). Finally, spectra of aragonite were obtained from a clam shell collected in a push core (PC#46) from Southern Hydrate Ridge during ROV *Tiburon* Dive #705 in July of 2004.

Samples were not "prepared" for Raman analysis in this study. In most cases, rock samples were analyzed without sawing, cleaning or polishing and no effort was made to optimize the Raman signal by adjusting the orientation of the mineral. The exceptions were the thin section containing isocubanite and samples of hydrothermal chimney wall that were cut to expose internal mineral gradients. Additionally, it should be noted that for most samples, the grain size of the minerals was smaller than the laser spot size of the instrument (<50 μm). The data obtained from these fine-grained, rough samples in the lab provide reasonable examples of what can be obtained from field deployments.

3.2. Laser Raman spectrometer

Laboratory measurements were performed with a Kaiser Optical Systems, Inc. (KOSI) laser Raman spectrometer which is equivalent to the sea-going DORISS instrument (Fig. 1). The NRxn spectrograph (used for both instruments) has a 50 μm slit and a duplex holographic grating. The collected light is dispersed into two "stripes", which are imaged with an Andor back-illuminated, TE-cooled, CCD camera. The CCD array is 2048×512 pixels. A 100 mW, frequency-doubled Nd:YAG (532 nm) laser is used as the excitation source.

The spectrometer and laser are connected to an optical probe head with fiber optic cables (excitation fiber — 62.5 μm; collection fiber — 100 μm). Holographic filtering in the probe head removes any Raman scattering generated in the excitation fiber, and rejects the Rayleigh scattered light from the collection fiber. The probe head can be used with a variety of sampling optics and can be integrated into a microscope. For this work, a KOSI MarkII probe head was integrated with a Leica DM LP microscope with a 10× objective (f/2.0, 5.8 mm working distance, ~50 μm spot size). A KOSI MR probe head (smaller and with higher throughput than the Mark II) was used in conjunction with a 6.4 cm working distance f/3.0 non-contact optic (NCO) and a 3 mm working distance f/2.0 immersion optic (IO), with laser spot sizes of ~200 μm and ~50 μm, respectively.

The spectral range of the spectrometer is 100–4400 Δcm^{-1}. For an excitation wavelength of 532 nm, this Raman shift corresponds to a
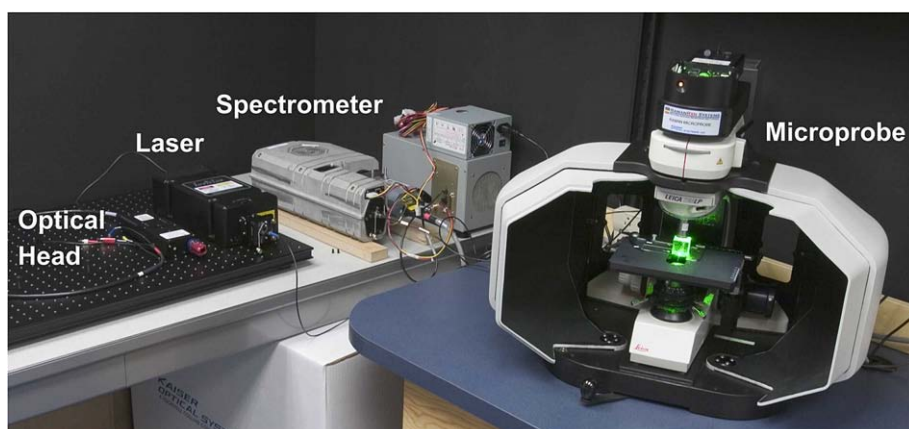

Fig. 1. Kaiser Optical Systems, Inc. laser Raman spectrometer and microprobe. The spectrometer is fiber-optically coupled to either the microprobe (right) or a remote optical head (left). A 532 nm Nd:YAG laser is used for excitation.

spectral region of 535–695 nm. The lower cutoff limit depends on the optical head. The cut-off for the Mark II probe head (integrated with the microscope) is ~ 150 Δcm^{-1}; the cut-off of the MR Probe is ~ 160 Δcm^{-1}. The duplex grating combined with a 2048 pixel wide CCD, leads to a mapping of ~ 1 cm^{-1}/pixel. The spectral resolution, which is affected by the slit width (50 μm), is ~ 5 cm^{-1} (determined by the full width at half maximum of neon spectral lines). Maximum laser power at the sample is ~ 20 mW through the microprobe, and ~ 40 mW through the NCO and IO. The decreased laser power (with respect to the 100 mW source) is due to loses from coupling with the fiber and filtering in the probe head. The spectrometer was calibrated for wavelength using a neon source, and for intensity using a halogen source. Calibration was verified daily with the ~ 520 Δcm^{-1} band of a polished silicon wafer.

Additional Raman measurements were made with an InPhotonics, Inc. portable InPhotote™ spectrometer with a red (785 nm) excitation source and 1024 × 128 pixel, TE-cooled CCD camera. The InPhotote has a spectral range of ~ 250–2350 Δcm^{-1}. For an excitation wavelength of 785 nm, this corresponds to a spectral region of 800–963 nm. The spectral resolution is 6–8 cm^{-1}. Approximately 10 mW of laser power was focused on the sample using a fiber optic probe head. The f/1.7 sampling optic had a 7.5 mm working distance. The InPhotote was also calibrated using a neon source.

The exposure times of the spectra were selected according to the sample (due to variations in Raman signal strength). The control software for the KOSI instrument (HoloGRAMS) enables a single spectrum to be obtained that is an average of 10 accumulations (which helps to reduce noise levels in the data) and filters out spikes in the data caused by cosmic ray events; the InPhotote control software only allows single accumulations to be acquired. It should be noted that all spectra in this study were obtained in air (unless otherwise noted). Previously collected in situ spectra did not show any effects from seawater, temperature or pressure on the Raman spectra of hydrothermal minerals (White et al., 2005, 2006b).

All spectra were analyzed using GRAMS/AI spectroscopic data processing software (Thermo Scientific). The Raman band position, height and area were determined using the GRAMS/AI peak fitting routine. This routine calculates a baseline, and then evaluates the peak above the baseline. It uses an iterative technique to fit mixed Gaussian–Lorentzian bands to the data and minimize the χ^2 (reduced chi-squared) value, which measures "goodness-of-fit".

4. Results — Raman spectra of minerals

Multiple spectra were obtained for each mineral using the variety of sampling optics described above. It should be noted that the spot location and orientation were not the same for each spectrum. In many cases a number of different individual grains were analyzed for each mineral. Peaks from minor mineral impurities could be identified in some of the spectra. The mineral bands listed in this paper (Tables 2–7) were consistently observed in all of the spectra acquired on the same mineral species. Band positions only varied by a few wavenumbers at most. This observed variation was due to non-uniqueness of results from the peak fitting routine (primarily for small bands with lower signal-to-

Table 2
Raman band positions (and normalized intensity) for sulfur for three different sampling configurations

Sulfur (S_8) — Mariana Arc Sample		
Microprobe 10× (green excitation)	MR Probe/NCO (green excitation)	InPhotote (red excitation)
153 (0.60)		
186 (0.05)		
219 (1.41)	219 (1.37)	
246 (0.11)	247 (0.07)	245 (0.08)
437 (0.09)	438 (0.09)	434 (0.12)
472 (1.00)	472 (1.00)	472 (1.00)

Table 3
Raman bands and normalized intensity for carbonate mineral standards and samples

Sample/source	Band position	Normalized intensity average (range)	Comment[a]
Calcite ($CaCO_3$)[b]	282	0.23 (0.06–0.31)	Librational lattice mode
Rock collection kit	713	0.09 (0.02–0.11)	CO_3 bending (ν_4)
	1086	1.00	CO_3 stretching (ν_1)
Aragonite ($CaCO_3$)[c]	155	0.19	Translational lattice mode
Seafloor shell from	207	0.24 (0.22–0.28)	Librational lattice mode
Hydrate Ridge	704	0.14 (0.12–0.16)	CO_3 bending (ν_4)
	1085	1.00	CO_3 stretching (ν_1)

[a] Bischoff et al., 1985; Urmos et al., 1991; Stopar et al., 2005.
[b] Six total spectra: 10× (1), NCO (3), IO (1), InPhotote (1).
[c] Six total spectra: 10× (1), NCO (2), InPhotote (2).

noise levels), and possibly due to slight compositional differences in the natural samples. The KOSI spectrometer itself provided consistent (within 1 cm^{-1}) band positions for each mineral species over long periods of time (months) regardless of the sampling optic used. Normalized band intensities (height of a given band divided by the height of the dominant band) showed greater variation (as much as 50% at times), mostly likely due to variations in crystal orientation. The order of normalized intensity among bands was very consistent for each mineral species. The normalized band intensities listed in the tables are averages of spectra obtained with different sampling optics and from different grains of a mineral sample; the ranges of normalized intensities observed are listed in parentheses. Not all of the bands were observed in each spectrum, particularly when signal strength was not sufficiently high to allow minor bands to be detected above the noise level. In some cases, recognized band positions were lower than the low-cut-off value for the optical head, thereby preventing detection of the band.

4.1. Elemental sulfur

An elemental mineral of interest in hydrothermal and other seafloor seep systems is sulfur. Sulfur-oxidizing bacteria, which provide a base for the chemosynthetic food web in these deep sea environments, produce filamentous sulfur (Taylor and Wirsen, 1997). Laboratory Raman studies by Pasteris et al. (2001) have identified elemental sulfur in the S_8 configuration in the bacteria *Thioploca* and *Beggiatoa*. In situ laser Raman spectroscopic measurements of

Table 4
Raman bands and normalized intensity for sulfate mineral standards and samples

Sample/source	Band position	Normalized intensity average (range)	Comment[a]
Anhydrite ($CaSO_4$)[b]	417	0.09 (0.05–0.15)	SO_4 bending (ν_2)
A-2178-3-1-Anh and	499	0.16 (0.04–0.22)	SO_4 bending (ν_2)
J2-137-1-R1-A	628	0.13 (0.07–0.16)	SO_4 bending (ν_4)
	675	0.09 (0.05–0.11)	SO_4 bending (ν_4)
	1017	1.00	SO_4 stretching (ν_1)
	1128	0.25 (0.14–0.30)	SO_4 stretching (ν_3)
	1160	0.09 (0.05–0.12)	SO_4 stretching (ν_3)
Gypsum ($CaSO_4–2H_2O$)[c]	415	0.12 (0.11–0.13)	SO_4 bending (ν_2)
Fisher Scientific	494	0.12 (0.10–0.14)	SO_4 bending (ν_2)
	620	0.06 (0.06–0.07)	SO_4 bending (ν_4)
	671	0.06 (0.06–0.07)	SO_4 bending (ν_4)
	1008	1.00	SO_4 stretching (ν_1)
	1136	0.17 (0.16–0.17)	SO_4 stretching (ν_3)
	3406	0.18 (0.15–0.20)	O–H stretching
	3494	0.25 (0.23–0.29)	O–H stretching
Barite ($BaSO_4$)[d]	452	0.15 (0.13–0.17)	SO_4 bending (ν_2)
Fisher Scientific	462	0.24 (0.21–0.26)	SO_4 bending (ν_2)
	617	0.08 (0.07–0.08)	SO_4 bending (ν_4)
	988	1.00	SO_4 stretching (ν_1)
	1141	0.07 (0.06–0.07)	SO_4 stretching (ν_3)

[a] Dickinson and Dillon, 1929; Stopar et al., 2005; Wiens et al., 2005.
[b] Seven total spectra: 10× (3), NCO (2), InPhotote (2).
[c] Six total spectra: 10× (1), NCO (3), IO (1), InPhotote (1).
[d] Six total spectra: 10× (1), NCO (3), IO (1), InPhotote (1).

Table 5

Anhydrite Raman band positions (and normalized intensity) from two samples using two different optics

A-2178-33-1-Anh (grain 2)		J2-137-1-R1-A	
10×	NCO	10×[a]	NCO[b]
417 (0.06)	417 (0.07)	418 (0.10)	417 (0.10)
499 (0.20)	500 (0.19)	500 (0.17)	500 (0.15)
628 (0.15)	628 (0.15)	628 (0.11)	628 (0.13)
675 (0.08)	676 (0.09)	676 (0.05)	676 (0.10)
1017 (1.00)	1017 (1.00)	1017 (1.00)	1017 (1.00)
1128 (0.25)	1128 (0.28)	1128 (0.14)	1129 (0.29)
1160 (0.12)	1160 (0.11)	1160 (0.09)	1160 (0.10)

[a] Black matrix.
[b] Grey inclusion near gold area.

bacterial mats at the Hydrate Ridge site have also detected the presence of S_8 sulfur (White et al., 2006b). Sulfur is also produced hydrothermally and in volcanic eruptions (Nakamura et al., 2006). The mineral sample analyzed here is not biogenic but has the same S_8 configuration as biogenic sulfur.

S_8 sulfur has an orthorhombic crystal structure and is a strong Raman scatterer. The dominant Raman bands of sulfur are at ~219 and 472 Δcm^{-1}. Additional minor bands are at ~153, 437, 246 and 187 Δcm^{-1} (Fig. 2). The bands in the 100–300 Δcm^{-1} region are due to S–S–S bending and the bands in the 400–500 Δcm^{-1} region are due to S–S stretching (Ozin, 1969; Harvey and Butler, 1986). The band positions and relative intensities for sulfur obtained with the microprobe/10×, MR Probe/NCO, and InPhotote (red excitation) are listed in Table 2. The relative intensities are listed with respect to the ~472 Δcm^{-1} band, which is the dominant band present in all three spectra. The 219 Δcm^{-1} band has a higher intensity than the band chosen for normalization, but it is not recorded by the InPhotote instrument due to its light rejection up to ~250 Δcm^{-1}. Pure sulfur has little fluorescence under either green or red excitation. The spectral data obtained in this study correspond

Table 6

Raman bands and normalized intensity for sulfide mineral standards and samples

Sample/source	Band position	Normalized intensity average (range)	Comment
Pyrite (FeS₂)[a]	343	0.89 (0.72–0.98)	
A-2178-3-1-Py	379	1.00	
	430	0.08 (0.07–0.09)	
Marcasite (FeS₂)[b]	323	1.00	
J2-135-5-R1-Mc	386	0.15 (0.08–0.26)	
Chalcopyrite (CuFeS₂)[c]	265	0.17 (0.10–0.25)	Cu–S band
A-2003-7-1a5, J2-137-1-R1-A,	291	1.00	Fe–S band
and Wards Natural Science	320	0.21 (0.09–0.33)	Fe–S band
	352	0.17 (0.08–0.24)	Fe–S band
	456	0.22 (0.06–0.44)	
	471	0.71 (0.09–1.36)	Cu–S band
Isocubanite (CuFe₂S₃)[d]	351	0.70 (0.65–0.79)	
2467 RO1 P14MC	386	1.00	
	441	0.11 (0.10–0.11)	
Sphalerite ((Zn,Fe)S)[e]	298	1.00	Fe–S band
Wards Natural Science	309	0.40 (0.33–0.43)	Fe–S band
	329	0.47 (0.42–0.52)	Fe–S band
	340	0.13 (0.12–0.17)	Fe–S band
	350	0.22 (0.07–0.38)	Zn–S band
Wurtzite ((Zn,Fe)S)[f]	294	1.00	Fe–S band
2944-3-s1-w1	308	0.38 (0.27–0.60)	Fe–S band
	326	0.83 (0.78–0.88)	Fe–S band
	352	0.12 (0.09–0.17)	Zn–S band
	1167	0.10 (0.09–0.10)	

[a] Five total spectra: 10× (1), NCO (4).
[b] Seven total spectra: 10× (3), NCO (4).
[c] Ten total spectra: 10× (7), NCO (3).
[d] Three total spectra: 10× (3).
[e] Six total spectra: 10× (5), IO (1).
[f] Five total spectra: 10× (2), NCO (3).

Table 7

Chalcopyrite Raman band positions (and normalized intensity) from one sample using three different optics

A-2003-7-1a5 (Chalcopyrite)				
10×		NCO		IO
265 (0.10)	266 (0.17)			267 (0.10)
291 (1.00)	291 (1.00)	291 (1.00)	291 (1.00)	291 (1.00)
320 (0.13)	320 (0.15)	322 (0.09)	320 (0.12)	320 (0.12)
352 (0.09)	352 (0.09)	353 (0.11)	354 (0.10)	351 (0.10)
456 (0.16)	458 (0.44)			
471 (0.66)	471 (1.36)	470 (1.1)	470 (0.81)	

well to data reported in the literature for elemental sulfur analyzed in the lab (Edwards et al., 1997) and filamentous sulfur produced by bacterial mats analyzed in the lab (Pasteris et al., 2001) and in situ on the seafloor (White et al., 2006b).

4.2. Carbonates

Calcite and aragonite are two of the polymorphs of calcium carbonate ($CaCO_3$), and both can be produced biologically. Calcite is trigonal, while aragonite has an orthorhombic crystal structure. Bivalve shells present at hydrothermal and cold seep sites are composed of calcium carbonate. Authigenic carbonate crusts are formed at cold seep sites and can contain calcite and high-Mg calcite. Laboratory Raman studies of individual shells have shown the presence of calcite and/or aragonite. In situ laser Raman spectroscopy measurements have also identified calcite and aragonite in shells on the seafloor (White et al., 2005, 2006b).

As shown in spectra of the mineral standards and natural samples analyzed in this study, the dominant Raman band of both common crystal structures of calcium carbonate is at ~1085 Δcm^{-1} due to the symmetric stretching (ν_1 vibration) of carbonate (CO_3). A minor, lattice mode band is also present at ~155 Δcm^{-1}. Because calcite and aragonite have different lattice structures, the positions of some of their minor Raman bands are different. Calcite has minor bands at ~282 and 713 Δcm^{-1}; aragonite has minor bands at ~207 and 704 Δcm^{-1} (Fig. 3). The bands below 300 Δcm^{-1} are lattice modes, while the bands near 700 Δcm^{-1} are due to the in-plane bending (ν_4 vibration) of CO_3 (Bischoff et al., 1985; Urmos et al., 1991; Stopar et al., 2005). A very weak band at ~1435 Δcm^{-1} for calcite and ~1462 Δcm^{-1} for aragonite was sometimes observed in spectra of sufficient signal strength; this is due to the anti-symmetric stretch (ν_3 vibration). The Raman band positions of both calcite and aragonite were very consistent regardless of the sampling optic or excitation wavelength. However, the normalized intensities (band height divided by the height of the ~1085 Δcm^{-1} band) showed some variation for calcite. This variation appeared to be somewhat related to the area being analyzed (i.e., whether the area was transparent or more opaque). Large, single, translucent crystals are more susceptible to optical scattering effects caused by anisotropy within the crystal. In opaque aggregates of fine grained crystals, the laser spot illuminates a large number of crystals in various orientations thus averaging out orientation effects. Spectra of aragonite were collected from both the inside and outside of the shell sample. Raman band positions and normalized intensities were very consistent for all of the aragonite spectra. Table 3 shows the band positions and the variations in normalized intensity for six spectra of each sample collected with the following optics: calcite — 10× (1), NCO (3), IO (1), InPhotote (1); aragonite — 10× (1), NCO (3), InPhotote (2).

The spectrum of geological calcite collected with green excitation shows an inclined baseline due to some fluorescence of the sample (Fig. 3). However, the intensity of the fluorescence is not sufficient to obscure the Raman bands. The broad fluorescence observed from calcite in this study peaks at ~2900 Δcm^{-1} (~629 nm) (not shown).
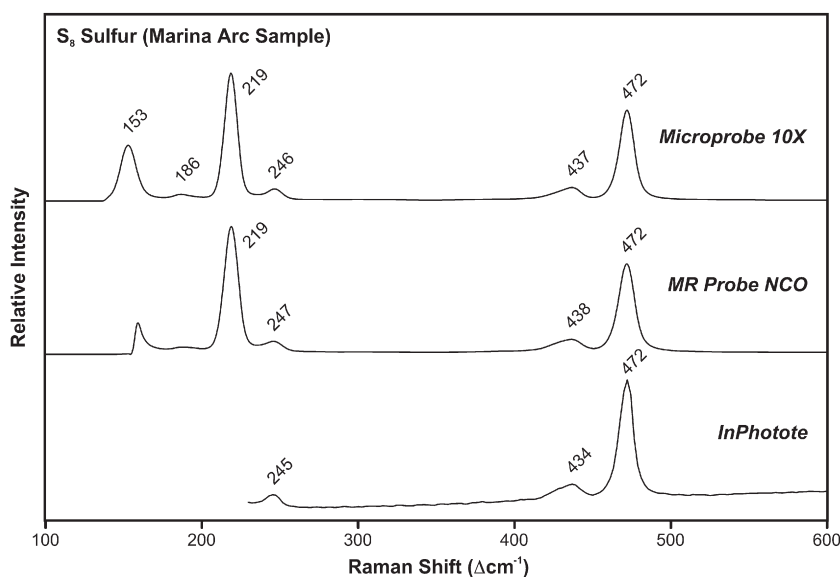
Fig. 2. Spectra of S_8 elemental sulfur: microprobe/10× (10×2 s exposure, green excitation); MR Probe/NCO (10×0.75 s exposure, green excitation); and InPhotote (1×5 s exposure, red laser excitation).

This fluorescence is most likely due to the presence of trace impurities in the sample. Calcite has long been known to be luminescent (Nichols et al., 1918) and red broadband emission (centered in the mid-600 nm region, as observed in this study) is due to the presence of trace amounts of Mn^{2+} (Marfunin, 1979; El Ali et al., 1993). Spectra obtained using red excitation do not show fluorescence (Fig. 3).

4.3. Sulfates

Anhydrite ($CaSO_4$) is precipitated in the first stage of chimney formation when Ca-rich hydrothermal fluids mix with Ca- and SO_4-rich ambient seawater. In the second stage, sulfide minerals precipitate along the chimney conduit and within interstices of previously precipitated anhydrite and sulfide grains, creating zonation sequences that reflect thermal and chemical gradients across the chimney wall (Goldfarb et al., 1983; Haymon, 1983; Tivey and McDuff, 1990; Tivey, 1995). At temperatures above 130 °C, seawater is saturated with respect to anhydrite (Haymon and Kastner, 1981). Thus, anhydrite is present in active, high-temperature chimneys. Over

time anhydrite can be altered to gypsum ($CaSO_4 \cdot 2H_2O$), or dissolved as the temperature drops below 130 °C.

Barite ($BaSO_4$) can be found as a minor component of high-temperature chimneys and a major component in some lower temperature chimneys (e.g., Hannington and Scott, 1988); however, larger deposits of barite can be found in other locations on the seafloor. The Tubeworm Slump site at a depth of 2310 m in Monterey Bay consists of a number of barite mounds (some as high as 1 m) in an area that is approximately 20 m in diameter (Naehr et al., 2000). Naehr et al. (2000) hypothesized that the site was the result of a sediment slump exposing barium-rich pore waters to sulfate-rich seawater. This site is similar to other cold-seep barite sites observed along continental margins (Torres et al., 2003) (e.g., at the San Clemente Fault (Lonsdale, 1979) and in the Sea of Okhotsk (Greinert et al., 2002)).

Raman spectra were collected from hydrothermal anhydrite samples and from gypsum and barite standards obtained from Fisher Scientific. Band positions and normalized intensities obtained in this study are listed in Table 4. The Raman bands of these minerals are due to the vibrations within sulfate tetrahedra (SO_4). Differences in the structures of these minerals and the different metals bonded to the
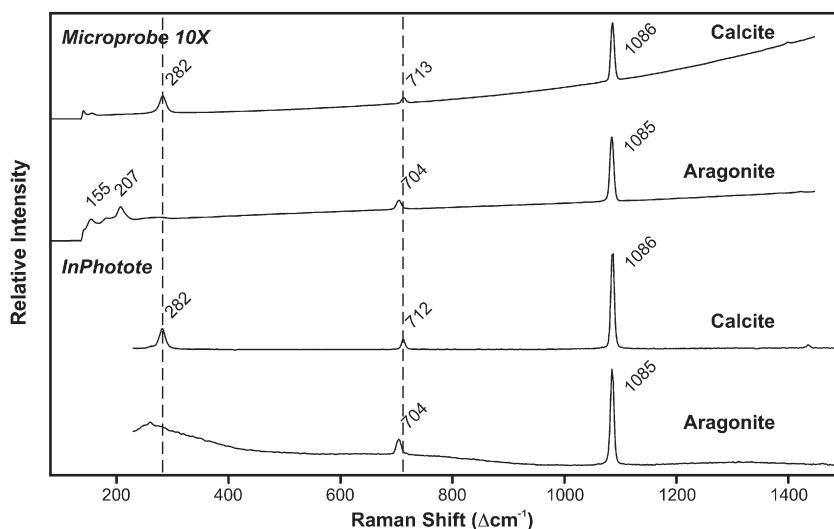

Fig. 3. Raman spectra of $CaCO_3$ — calcite (rock collection sample #6) and aragonite (seafloor shell). The upper two spectra were obtained with the microprobe (10× objective) using green excitation; spectra are 10×1 s exposures for calcite, and 10×7 s exposures for aragonite. The lower two spectra were obtained with the InPhotote using red excitation; spectra were single 20 s exposures for calcite, and 30 s for aragonite.

sulfate ion (or the presence of H_2O) cause slight differences in the position of the Raman bands (Fig. 4a). The dominant Raman band is due to the symmetric stretching (ν_1 vibration) of SO_4 and is located at $\sim 1000 \Delta cm^{-1}$: $\sim 1017 \Delta cm^{-1}$ for anhydrite, $\sim 1008 \Delta cm^{-1}$ for gypsum, and $\sim 988 \Delta cm^{-1}$ for barite. The intensities of all bands were normalized by dividing each peak height by the peak height for this dominant band. The ν_2 vibration (in-plane bending) generates bands in the 400–500 Δcm^{-1} region, the ν_4 vibration (out-of-plane bending) generates bands in the 600–700 Δcm^{-1} region, and the ν_3 vibration (asymmetric stretching) generates bands in the 1100–1200 Δcm^{-1} region. Due to the incorporation of water molecules, gypsum also has O–H stretching bands at ~ 3406 and $3494 \Delta cm^{-1}$ (not shown) which were detected using the KOSI instrument under green excitation.

Anhydrite spectra were collected from relatively pure anhydrite grains (A2178-3-1-Anh) and from sample J2-137-1-r1-a, which is a sample from a chimney wall (Fig. 5). Anhydrite is located throughout sample J2-137-1-r1-a as visible inclusions (~ 0.5 mm) and incorporated in a black matrix of ZnS. Table 5 compares Raman band positions and normalized band intensities for both of these samples obtained with the 10× and NCO sampling optics. The band positions and normalized intensities are very consistent for both the non-mineralic anhydrite samples and anhydrite incorporated in a matrix of other minerals. The data obtained in this study also correspond well to values found in the literature (e.g., Dickinson and Dillon, 1929; Stopar et al., 2005; Wiens et al., 2005).

No fluorescence is observed in the sulfate spectra using a green excitation laser (Fig. 4a) or in the gypsum or barite spectra using a red excitation laser (Fig. 4b). However, the spectrum of anhydrite acquired using red excitation contains non-Raman bands in the 1200–1800 Δcm^{-1} region (only two of these bands are shown in Fig. 4b). These may be fluorescence bands due to impurities or trace materials in the hydrothermal anhydrite. No significant impurity phases or discolorations were visible under the microscope, but the presence of Mn and rare earth elements has been shown to produce luminescent bands in natural anhydrite (Marfunin, 1979).

4.4. Sulfides

High-temperature black smoker chimneys are dominated by sulfide phases, in addition to the previously mentioned anhydrite. The
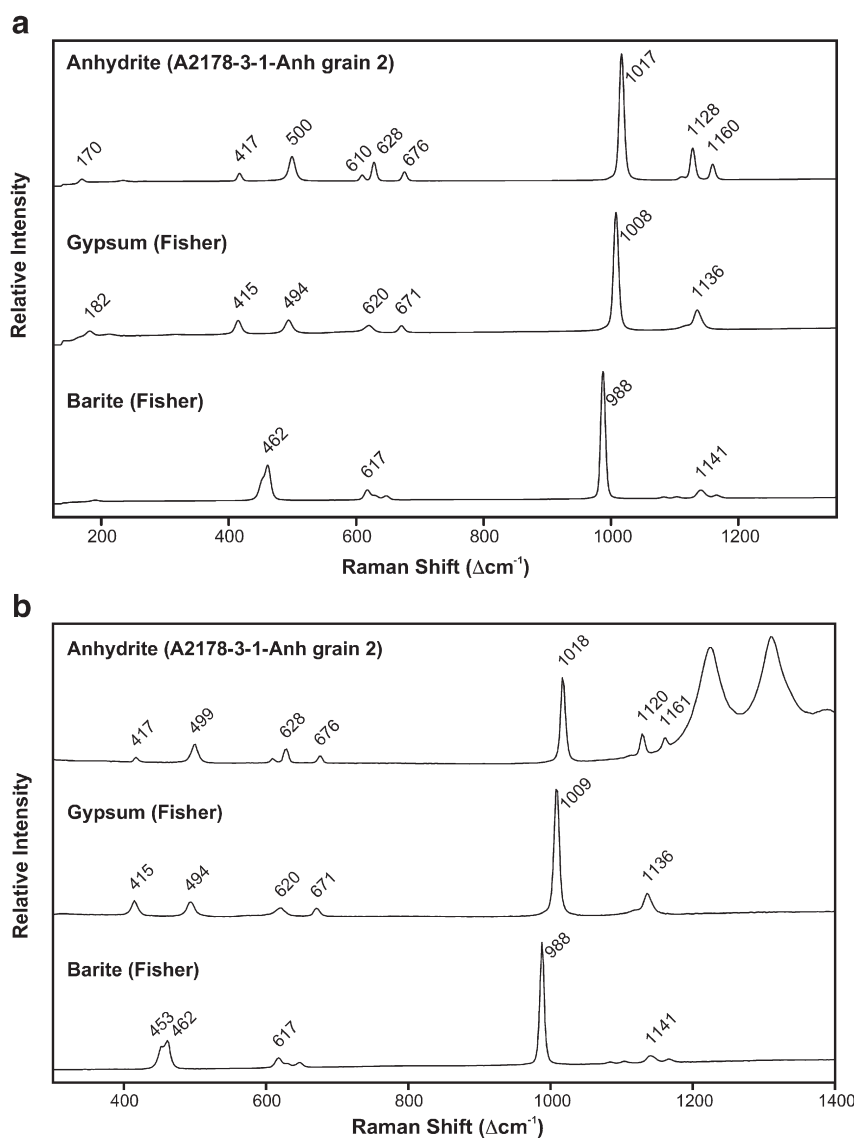

Fig. 4. a. Raman spectra of sulfates obtained with the microprobe (10× objective) and green excitation. The anhydrite spectrum is 10×10 s; the gypsum spectrum is 10×20 s; and the barite spectrum is 10×7 s. b. Raman spectra of sulfates obtained with the InPhotote and red excitation. All spectra are single exposures of 10 s for anhydrite and barite, and 30 s for gypsum.

Fig. 5. Hydrothermal chimney samples from an active open conduit smoker, Kilo Moana vent field, Eastern Lau Spreading Center (J2-137-1-R1-A) and from an inactive chimney from 11N on the East Pacific Rise. (From WHOI seafloor sulfide collection, M.K. Tivey).

major phases include chalcopyrite ($CuFeS_2$), pyrite (FeS_2), and polymorphs sphalerite and wurtzite ($(Zn,Fe)S$)). Additional, minor sulfide phases include marcasite (FeS_2), pyrrhotite ($Fe_{(1-x)}S$), and isocubanite ($CuFe_2S_3$) (e.g., Haymon and Kastner, 1981; Rona et al., 1986; Tivey and Delaney, 1986). Most of these sulfides are Raman active (Fig. 6). Pyrrhotite has variable composition, and two structural forms — hexagonal and monoclinic. A number of bands were observed in pyrrhotite spectra obtained in this study. However, based on theoretical derivations (Mernagh and Trudu, 1993; Kroumova et al., 2003), none of the vibrational modes of either form of pyrrhotite are Raman active. Some of the bands observed appear to be due to sulfur and sulfate impurities; the remaining bands are likely the result of narrow band fluorescence and are highly variable.

The Raman bands of sulfide minerals identified in this study and their normalized intensities are listed in Table 6. The Raman signal strength for sulfides was lower than that of the minerals previously discussed. Due to the lower signal-to-noise and the fact that some of the bands overlap one another, the Raman band positions sometimes varied up to a few wavenumbers in analyses of different samples of the same mineral. However, this did not prohibit proper mineral

identification. Mernagh and Trudu (1993) investigated a number of primarily terrestrial sulfides using a 514 nm Ar ion laser as the excitation source. The data in this work corresponds well to Mernagh and Trudu (1993) and other previous work on terrestrial samples (e.g., Ushioda, 1972; Turcotte et al., 1993; Pasteris, 1998; Wang et al., 2004).

Pyrite and marcasite are polymorphs of FeS_2 (Fig. 6); pyrite has a cubic symmetry while marcasite is orthorhombic. Pyrite has two dominant Raman bands at ~343 and 379 Δcm^{-1}, and a minor band at ~430 Δcm^{-1} (Table 5). These bands correspond to the A_g, E_g, and $T_g(3)$ vibrational modes, respectively. By deconvolving the dominant observed peaks, two minor bands are also observed at ~350 and 377 Δcm^{-1} (the $T_g(1)$ and $T_g(2)$ vibrational modes) (Ushioda, 1972; Blanchard et al., 2005). Spectra obtained on marcasite (particularly with the microprobe) often showed additional mineral species such as barite and anhydrite, which presumably were intergrown on a fine scale. The dominant bands that appear to be those of marcasite are ~323 and 386 Δcm^{-1} (Table 6). These bands correspond to those identified in the literature, which have been assigned to the A_g stretching mode (Lutz and Müller, 1991; Mernagh and Trudu, 1993). An additional band at ~394 Δcm^{-1} was observed in many of the spectra as a minor shoulder of the 386 Δcm^{-1} band. Lutz and Müller (1991) also observe this band in some spectra and associate it with the B_{1g} librational mode. The Raman spectra of pyrite and marcasite obtained with the red excitation laser were much weaker in intensity than those obtained with the green laser, but the dominant bands (~343 and 379 Δcm^{-1} for pyrite, and ~323 and 386 Δcm^{-1} for marcasite) were observed.

Chalcopyrite ($CuFeS_2$) has a tetragonal crystal structure. There are few data in the literature on the Raman spectrum of chalcopyrite. Spectra obtained on chalcopyrite in this work were occasionally contaminated by the presence of sulfates such as barite. Unlike other minerals in this study, chalcopyrite spectra were collected from both homogeneous samples obtained from Ward's Natural Sciences and two chimney wall samples (Fig. 5) that clearly show the zonation from a chalcopyrite-rich "inner" conduit wall outward to a Zn–S matrix. Trace amounts of sulfates are also present throughout the chimney samples. Due to the strong Raman scattering of sulfates, a minor amount of a sulfate in the beam path can create significant peaks in the spectrum. The characteristic peaks of chalcopyrite include a dominant band at ~291 and minor bands at ~265, 320, and 352 Δcm^{-1} (Table 6, Fig. 6). These bands correspond to those observed by Mernagh and Trudu (1993). A large band at ~471 Δcm^{-1} was often observed in the spectra from the chimney samples which varied in intensity with respect to the other Raman bands. While it is similar in position to the strong sulfur band (~474 Δcm^{-1}), the lack of the 219 Δcm^{-1} sulfur band suggests that the 471 band is not due to the presence of trace amounts of sulfur. The University of Arizona's online RRUFF database (Downs, 2006) contains spectra from four samples of chalcopyrite. The ~471 Δcm^{-1} band is
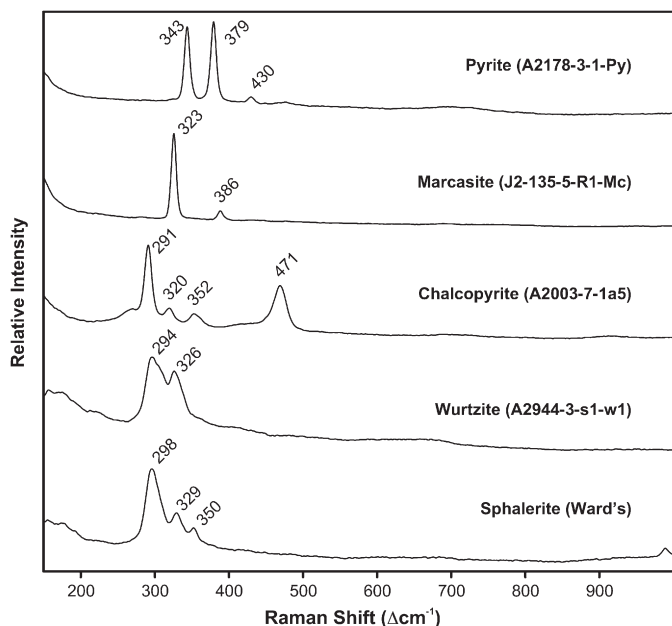

Fig. 6. Raman spectra of sulfides obtained with the microprobe (10× objective) using green excitation. The pyrite, marcasite, chalcopyrite and wurtzite spectra are all 10×60 s exposures; marcasite is 10×15 s.

present in some of these spectra, but not others. In this study, the intensity of the 471 band is higher for the A2003-7-1a5 sample than for the J2-137-1-r1-a sample (0.92 averaged normalized intensity for sample A2003-7-1a5 compared to 0.14 for sample J2-137-1-r1-a). The 265 and 471 Δcm^{-1} bands are Cu–S bands (Smith and Clark, 2002; Branch et al., 2003). Thus, the higher intensity observed in one sample may be due to the presence of Cu–S tarnishes present on the sample. This is discussed in more detail in the next section. Table 7 lists the band positions and normalized intensity for spectra of sample A2003-7-1a5 collected using the 10× objective, NCO, and IO sampling optics (all using green excitation). Not all of the bands were observed in each case. As stated above, the 471 Δcm^{-1} band shows great variability in normalized intensity.

Sphalerite and wurtzite ((Zn,Fe)S) are polymorphs of zinc sulfide whose crystal structures accommodate a number of replacements for zinc, including iron. Sphalerite has a cubic crystal structure, and wurtzite is hexagonal. The sphalerite sample has Raman bands at ~298 (dominant), 309, 329, 340, and 350 Δcm^{-1} (Table 6, Fig. 6). The ~350 band is a Zn–S band, whereas the lower wavenumber bands are Fe–S bands. The normalized band intensities observed in this study correspond to those for low-Fe sphalerite (~7 wt.% Fe, ~57 wt.% Zn in Kharbish (2007)). Wurtzite has similar band positions at ~294, 308, 326, and 352 Δcm^{-1} (Table 6, Fig. 6), which correspond to data in Mernagh and Trudu (1993). Within the individual sphalerite and wurtzite spectra, the Raman bands are quite close together, such that some of the minor bands are not resolved in the raw spectra. The individual bands can be identified by deconvolving the spectra with a peak-fitting program (such as GRAMS/AI).

Isocubanite ($CuFe_2S_3$) is a cubic structured polymorph of cubanite (previously referred to as *iss*-cubanite) (Caye et al., 1988). Samples of isocubanite (identified by petrographic microscope under reflected light) were analyzed in thin section using the Raman microprobe (10× objective). The use of micro-Raman spectroscopy to analyze minerals in thin section was described by Mao et al. (1987). Two primary Raman bands are observed at ~351 and 386 Δcm^{-1} (Table 6, Fig. 7). A minor, broader band is also observed at ~441 Δcm^{-1}. This sample was not analyzed with the NCO or IO remote optics, or with red excitation.

Raman spectra of the other sulfides were also obtained with red excitation. However, while all of the characteristic peaks were observed, the signal strengths were significantly lower (and thus noisier) than with green excitation. Peak fits for these data were not included in Table 6 due to the low signal quality.

5. Application — Raman spectra of recovered hydrothermal chimney samples

The data obtained in this study were applied to the analysis of two chimney wall samples. The NCO sampling optic (with green excitation) was used to collect Raman spectra in a profile across visible zonation patterns of each sample to identify the mineral species present.

5.1. Sample J2-137-1-r1-a

This sample is a portion of a chimney wall recovered from the Kilo Moana vent field on the Eastern Lau Spreading Center (Tivey et al., 2005). The "inner" wall is dominated by a gold-colored mineral, while the "outer" section is dominantly black in color. A series of seven spectra was collected with the MR Probe/NCO across the sawn sample face shown in Fig. 5. Five representative spectra from this scan are shown in Fig. 8. The spectrum from the outer-most portion (furthest from the gold) contains Raman bands indicating the presence of wurtzite (~296, 308 and 330 Δcm^{-1}) and pyrite (~346 and 378 Δcm^{-1}) (Fig. 8a). Moving towards the gold region the spectra are dominated by sphalerite with some pyrite and/or anhydrite (Fig. 8b,c). A spectrum was collected from a white inclusion in the gold region, which was primarily anhydrite (Fig. 8d). Moving into the gold region toward the "inner" rim of the sample, the spectra are dominated by chalcopyrite (~291, 320, 352 Δcm^{-1}) (Fig. 8e).

The Raman spectra agree reasonably well with visual observations from a thin section taken from the same chimney: the chimney conduit is lined with cubanite or chalcopyrite, grading out to intermediate solid solution (intergrowths of cubanite and chalcopyrite lamellae) with minor inclusions of pyrite; there is then an abrupt transition to a mixture of wurtzite with minor chalcopyrite, pyrite, and anhydrite, with outermost portions a mixture of sphalerite and/or wurtzite, pyrite, and amorphous silica with minor anhydrite present.

Sulfate bands were observed in many of the spectra near ~990 Δcm^{-1} (with attendant minor bands in the 400 and 600 Δcm^{-1} regions). However, no visible grains of sulfate minerals (other than anhydrite) were observed in this sample under the microprobe using reflected light or in the thin section from the same chimney viewed with a petrographic microscope. Given that this sample was recovered and removed from seawater and dried without any prior rinsing, it is possible that the sulfate bands observed are due to fine-grained sulfate salts precipitated from seawater on the surface and in interstitial spaces. Sulfates such as $CuSO_4$, $FeSO_4$, $MgSO_4$, $MnSO_4$, KSO_4, $NaSO_4$, and $ZnSO_4$ all have primary Raman bands in the ~975 to 1025 Δcm^{-1} region. To test the above hypothesis, a piece of the same chimney wall was soaked in distilled water and then rinsed and dried. A white precipitate was present on most surfaces after drying, and Raman analyses of these areas produced sulfate bands, though at slightly different band positions. This is consistent with different sulfate salts having reprecipitated during drying. The sample was then placed in deionized water. Raman analyses of the submerged sample were performed (using the microprobe with 10× objective), and clear sulfide bands were observed at ~299, 330 and 351 Δcm^{-1}. The only "extra" band observed in the ~400 to 1200 Δcm^{-1} region was at 981 Δcm^{-1}, which is the location of the dissolved sulfate ion band. These analyses support the initial hypothesis that the bands in the original sample do indeed represent precipitated salts from interstitial seawater.
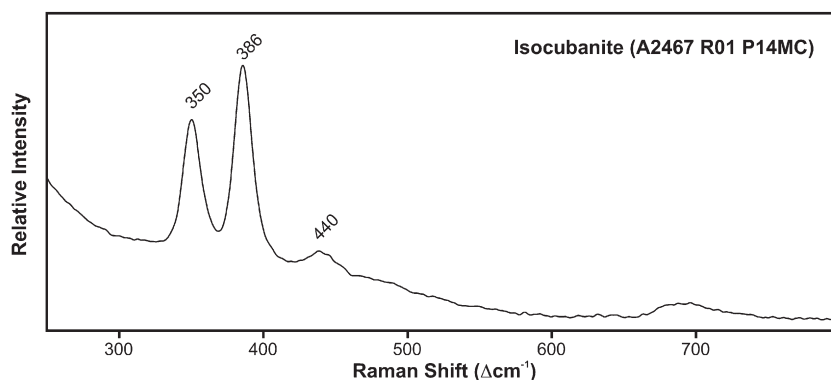

Fig. 7. Raman spectrum of isocubanite obtained from a thin section using the microprobe (10× objective) and green excitation. The spectrum is a 10×30 s exposure.
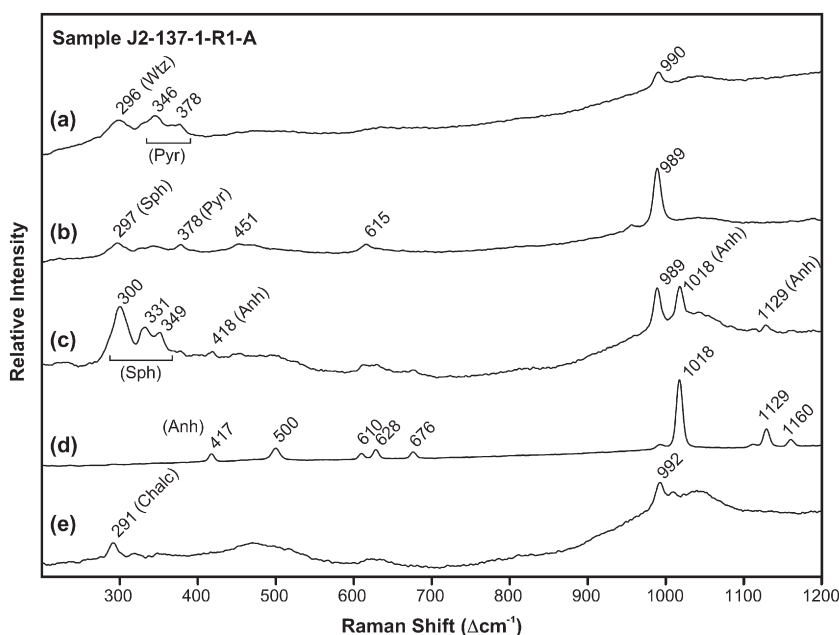
Fig. 8. Scan of spectra across the sample J2-137-1-r1-a (Fig. 5) using the NCO and green excitation. Spectra (a), (b) and (c) are from the black-colored region of the sample; spectrum (d) is from a white inclusion, spectrum (e) is from the gold-colored region. Mineral peaks are identified as wurtzite (Wtz), pyrite (Pyr), sphalerite (Sph), anhydrite (Anh) and chalcopyrite (Chalc). All spectra are 10×15 s exposures.

Sulfate minerals are strong Raman scatters compared to sulfides. Therefore, even a small amount of precipitated sulfate can produce a visible Raman band during long exposures. This is not an issue for in situ analyses. However, if recovered samples are analyzed using laser Raman spectroscopy, the likely presence of dried salts needs to be considered when interpreting data.

5.2. Sample A2003-7-1a5

Sample A2003-7-1a5 is from an inactive sealed chimney recovered from 11°N on the East Pacific Rise in 1988. Bands of tarnish are observed on one side of the sample (Fig. 5). These tarnishes vary in color from black to bluish-green to purple, and are assumed to be a progression from bornite (Cu_5FeS_4) to covellite (CuS) to chalcocite (Cu_2S) to digenite (Cu_9S_5) — losing Fe and gaining Cu (Tivey, pers. comm.). Spectra were obtained from an untarnished region of the sample and from the blackish, bluish-green, and purplish regions of the tarnish (Fig. 9). The spectrum from the untarnished

region was clearly chalcopyrite with band positions (and normalized intensities) of: ~291 (1.00), 320 (0.21), 354 (0.26) and 470 (0.91) Δcm^{-1}. Moving from the purplish tarnish to the blackish tarnish, Cu–S bands at ~265 and 472 Δcm^{-1} increase in intensity, while the Fe–S bands at ~291, 320, and 354 Δcm^{-1} decrease in intensity. The Raman spectrum of covellite (Cu–S) is characterized by a dominant band at ~472 Δcm^{-1} and a minor band at ~264 Δcm^{-1} (Mernagh and Trudu, 1993; Smith and Clark, 2002). Mernagh and Trudu (1993) were unsuccessful in obtaining Raman spectra from bornite, chalcocite and digenite. The covellite band positions correspond to the Cu–S bands of chalcopyrite (Table 6). It is not clear whether the Fe–S bands observed in the purplish and bluish-green tarnish spectra are due to the presence of Fe in the tarnish (e.g., bornite tarnish), or if they are due to the underlying chalcopyrite. Two pyrite bands (344 and 378 Δcm^{-1}) are also visible in the spectrum from the purplish tarnish (underlined in Fig. 9). The Raman spectrum of the blackish tarnish (which may be more successful in covering the underlying chalcopyrite) suggests that it is a pure CuS mineral (i.e., covellite, chalcocite, or digenite).
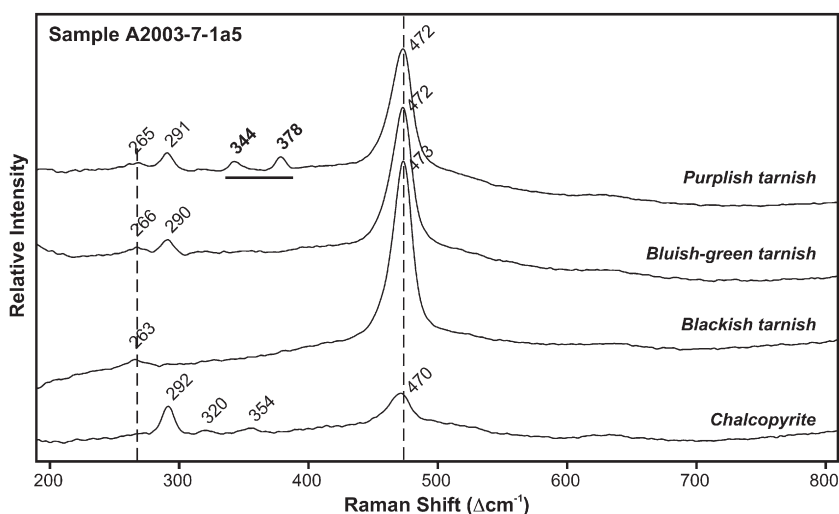

Fig. 9. Scan of spectra across the tarnishes on sample A2003-7-1a5 (Fig. 5) using the NCO and green excitation. The chalcopyrite spectrum (bottom) was collected from an area on the sample away from the tarnishes. All spectra are 10×15 s exposures.

6. Discussion

The data in this paper show that laser Raman spectroscopy is a powerful tool capable of identifying hydrothermal vent and cold seep minerals and distinguishing them from one another. The technique can be applied in the lab on whole samples, or thin sections, which is useful for fine-grained intergrowths and inclusions or for in situ analysis (e.g., White et al., 2006b). The data obtained in this study (characteristic band positions and normalized intensities) can be used with a computer algorithm such as RaSEA (Breier et al., submitted for publication) for automated mineral identification.

6.1. Relative Raman signal strength

The intensity of the Raman signal is a function of laser power, laser wavelength, and the Raman scattering efficiency of the sample. Sulfur is a strong Raman scatterer with a Raman scattering intensity an order of magnitude greater than that of the carbonates and sulfates. The sulfides produced the weakest Raman signal — three orders of magnitude lower than sulfur. This variation in Raman signal strength explains why small amounts of sulfur or sulfate minerals can produce observable peaks in a sulfide sample (e.g., Fig. 8). Additionally, more transparent minerals (such as anhydrite) may allow greater laser penetration and greater scattering within the sample than more opaque minerals (such as pyrite). In the former, the scattering volume is greater, resulting in a greater Raman signal.

6.2. Excitation wavelength

When recorded as the Raman shift, the band position in a Raman spectrum is not dependent on excitation wavelength. Typical excitation wavelengths include 514 nm (Ar ion laser), 532 nm (frequency doubled, Nd:YAG laser), 633 nm (He Ne laser), 785 nm (diode laser) and 1064 nm (Nd:YAG laser). However, Raman scattering *intensity* is inversely proportional to λ^4, so 532 nm produces a stronger Raman signal than 785 or 1064 nm. Green lasers (532 nm) are ideal for ocean work because this wavelength corresponds to the transmission peak of water. The previously mentioned DORISS instrument (Brewer et al., 2004; Pasteris et al., 2004) and aircraft-based Raman instruments (Leonard et al., 1979; Becucci et al., 1999) used 532 nm lasers. For an in-water working distance of 1 cm, 99.95% of 532 nm laser power will be transmitted compared to 97% of 785 nm laser power. However, for a 15 cm working distance, 99.25% of 532 nm laser power will be transmitted while only 64% of 785 nm laser power will be transmitted. The backscattered radiation will also be attenuated by a similar amount.

The disadvantage of an excitation source in the blue–green is that fluorescence can be generated by trace metals in minerals and by some organic materials. For example, fluorometers designed to measure *chlorophyll a* excite in the blue region (~ 440–470 nm) and detect fluorescence in the red (~ 685 nm). Methods for overcoming fluorescence are discussed by Ferraro et al. (2003) and include: changing the excitation wavelength (into the red); using pulsed lasers to discriminate the signals by time (Raman scattering is faster in response and shorter-lived than fluorescence (Matousek et al., 1999, 2001)); and exposing the sample to prolonged laser irradiation to bleach out fluorescent impurities.

Spectra obtained from natural samples as a part of this study demonstrate that hydrothermal minerals such as carbonates, sulfates, and sulfides do not suffer from significant fluorescence when analyzed with green excitation. Use of red excitation also produced spectra with distinct Raman peaks. However, in the case of anhydrite, red excitation resulted in additional peaks most likely due to fluorescence from minor impurities. The use of red excitation also resulted in lower signal strengths (after accounting for differences in laser power).

6.3. Sampling optics

Most of the samples were analyzed using three different sampling optics: 1) the microprobe with the 10× objective, 2) the MR remote probe head with the non-contact optic (NCO), and 3) the MR remote probe head with the immersion optic (IO). MBARI's DORISS instrument is capable of using both an NCO behind a dome window and an IO (Brewer et al., 2004). The optics with shorter working distances (10× and IO; 5.8 and 3 mm, respectively) have a shorter depth of focus, smaller laser spot size, and a higher power density at the sample. The NCO has a longer working distance (6.4 cm), a longer depth of focus, and a lower power density. Note that all of this work was done in air. In water, the working distance and depth of focus will be slightly greater. However, even in water, the depth of focus is small enough that some mechanism of focusing or positioning the laser spot (White et al., 2005) is needed.

It is difficult to compare the efficiencies of the optics because the signal intensity is affected by a number of factors. The most obvious factors are laser power and exposure time. The data were normalized by dividing the spectra by exposure time and laser power to account for these variations. Another factor to consider when selecting a sampling optic is proper positioning. For opaque samples, the focal point of the laser must be positioned at the surface of the sample. The depth of focus for the optics used here range from millimeter to sub-millimeter. The microscope objective could be focused visually by sighting through the objective via a camera. The remote head optics, however, do not have through-the-lens visualization capabilities and were focused by adjusting the position of the sample to maximize peak heights in the spectra. For solid samples, crystal orientation can also have an impact on the signal strength and depth of penetration into the sample. These variations cannot be accounted for quantitatively.

Spectra were compared by looking at normalized peak height (divided by exposure time and laser power) of the dominant band and relative order of peak intensities for the minor bands. In general, the normalized peak heights of spectra obtained from the three optics were around the same order of magnitude. The IO consistently provided greater intensities than the NCO. This enhanced signal is expected due to the higher power density it provides. The IO and 10× objective also have a slightly larger numerical aperture than the NCO (.25 vs. .17). The relative order of peak intensities of the minor bands was also consistent for all of the sampling optics used.

7. Conclusion

Laser Raman spectroscopy is a powerful tool for identifying mineral species in situ in the deep ocean. It is capable of obtaining high quality spectra of hydrothermally- and cold seep-relevant minerals such a carbonates, sulfates, and sulfides down to grain sizes below 50 μm. In order to build a sea-going instrument optimized for mineral analyses at these types of seafloor sites, detailed laboratory work must be performed to evaluate how readily the minerals of interest can be distinguished spectroscopically and to understand how the spectra are affected by natural variation in mineral chemistry and differences in instrument parameters.

High quality Raman spectra were obtained from standards and naturally occurring mineral samples using both red and green excitation. Although organic compounds and impurities have the potential to produce fluorescence (particularly with blue–green excitation), which can overwhelm the Raman signal, fluorescence was not observed to be a significant problem for any of the samples analyzed here. The highest quality spectra (highest signal-to-noise) were obtained using green excitation (532 nm Nd:YAG laser) and a sampling optic with a short depth of focus (and thus high power density). Sulfur was the strongest Raman scatterer, followed by the carbonates and sulfates. The sulfide minerals were the weakest Raman scatters, but good quality spectra were obtained from these minerals

as well. Characteristic Raman bands (and their relative intensities) were identified for each mineral (Tables 2–7), which correlated well with and built upon data found in the literature.

Based on the data from this work, a Raman system optimized for hydrothermal and cold seep minerals should have a spectral range of $100–1800 \, \Delta cm^{-1}$. All of the characteristic Raman bands of the minerals analyzed fall within this range, as does the $1640 \, \Delta cm^{-1}$ water bending band (against which Raman-active dissolved species can be normalized). The selection of a small spectral range also allows for higher spectral resolution. Because many of the sulfide minerals have Raman bands that are very close in wavenumber, an instrument resolution of $\leq 3 \, cm^{-1}$ would be preferable. 532 nm is the preferred excitation wavelength for the minerals analyzed in this work (particularly sulfates), because it produces a strong Raman signal and does not generate significant fluorescence. If organic materials (e.g., sediments) are present on the surface of the sample of interest, some type of brushing or scraping may be required to clean the surface before Raman spectra are obtained. Green excitation also allows greater in-water stand-off distances without significant attenuation of the signal. Use of a sampling optic with a 10 cm working distance (focal length) will decrease the possibility of accidentally touching the optic to the side of a chimney, which can be ~ 350 °C. A longer focal length optic will also have a longer depth of focus, which makes positioning of the focal point on the surface of the target easier. However, if work is to be done in areas of high sediment deposition or on hydrothermal plume particles that have organics present, then a 785 nm excitation laser with a ~ 1 cm working distance is preferable.

Operational challenges include positioning of the optical head, visualization of the area analyzed, and automation. Due to the small depth of focus of all of the sampling optics described, some form of positioner will be required to locate the laser spot on the target of interest. The three-degree-of-freedom Precision Underwater Positioner (White et al., 2005) developed for the DORISS instrument is an example of the type of system needed. For long-term Raman deployments at hydrothermal vents, positioning will be a challenge, as vent deposit topography can change rapidly over time. User control through an ROV or seafloor cable is simplest, but at some time a mechanism for automated positioning may be required. Regardless of how the optical head is positioned, visualization of the site – both on the scale of an individual chimney and on the scale of the measurement being made – is required to provide context for the spectra obtained.

The ability of laser Raman spectroscopy to optically identify mineralogy in situ makes it an ideal instrument for extreme environments such as other planets and the deep ocean. Planetary and oceanic explorations require similar characteristics such as small size, low power, robustness, etc. Wang et al. (1998, 2003) have developed a small-scale prototype for a Mars mission. The DORISS instrument (Brewer et al., 2004) is the first step in using Raman spectroscopy in the deep ocean. The development of new, smaller, smarter Raman instruments will greatly improve our understanding of mineralogic and geochemical processes occurring in these remote locations.

Acknowledgements

References

Aloisi, G., et al., 2000. Methane-related authigenic carbonates of eastern Mediterranean Sea mud volcanoes and their possible relation to gas hydrate destabilisation. Earth Planet. Sci. Lett. 184, 321–338.

Aloisi, G., et al., 2002. CH4-consuming microorganisms and the formation of carbonate crusts at cold seeps. Earth Planet. Sci. Lett. 203, 195–203.

Alt, J.C., 1995. Subseafloor processes in mid-ocean ridge hydrothermal systems. In: Humphris, S.E., Zierenberg, R.A., Mullineaux, L.S., Thomson, R.E. (Eds.), Seafloor Hydrothermal Systems: Physical, Chemical, Biological, and Geological Interactions. AGU, Washington, DC.

Baker, E.T., German, C.R., 2004. On the global distribution of hydrothermal vent fields. In: German, C.R., Lin, J., Parson, L.M. (Eds.), Mid-ocean Ridges: Hydrothermal Interactions Between the Lithosphere and Oceans. AGU, Washington, DC.

Becucci, M., Cavalieri, S., Eramo, R., Fini, L., Materazzi, M., 1999. Accuracy of remote sensing of water temperature by Raman spectroscopy. Appl. Opt. 38 (6), 928–931.

Bischoff, W.D., Sharma, S.K., Mackenzie, F.T., 1985. Carbonate ion disorder in synthetic and biogenic magnesian calcites: a Raman spectral study. Am. Mineral. 70, 581–589.

Blanchard, M., et al., 2005. Electronic structure study of the high-pressure vibrational spectrum of sFeS2 Pyrite. J. Phys. Chem. B 109, 22,067–22,073.

Branch, M.S., Berndt, P.R., Botha, J.R., Leitch, A.W.R., Weber, J., 2003. Structure and morphology of CuGaS2 thin films. Thin Solid Films 431–432, 94–98.

Breier, J.A., German, C.R., White, S.N., submitted for publication. Quantitative Mineral Speciation of Deep-Sea Hydrothermal Particulates by Raman Spectroscopy and Expert Algorithm (RaSEA) Point Counting: Towards Autonomous In Situ Exploration and Experimentation. Geochem. Geophys. Geosyst.

Brewer, P.G., et al., 2004. Development of a laser Raman spectrometer for deep-ocean science. Deep-Sea Res. I. doi:10.1016/j.dsr.2003.11.005.

Caye, R., et al., 1988. Isocubanite, a new definition of the cubic polymorph of cubanite CuFe2S3. Mineral. Mag. 52, 509–514.

Daly, K.L., et al., 2004. Chemical and biological sensors for time-series research: current status and new directions. MTS J. 38 (2), 121–143.

Dickinson, R.G., Dillon, R.T., 1929. The Raman spectrum of gypsum. Proc. Natl. Acad. Sci. 15 (9), 695–699.

Downs, R.T., 2006. The RRUFF Project: an integrated study of the chemistry, crystallography. Raman, and Infrared Spectroscopy of Minerals, 19th General Meeting of the International Mineralogical Association, Kobe, Japan, pp. O03–O13.

Edwards, H.G.M., Farwell, D.W., Turner, J.M.C., Williams, A.C., 1997. Novel environmental control chamber for FT-Raman spectroscopy: study of in situ phase change of sulfur. Appl. Spectrosc. 51 (1), 101–107.

El Ali, A., et al., 1993. Mn2+-activated luminescence in dolomite, calcite and magnesite: quantitative determination of manganese and site distribution by EPR and CL spectroscopy. Chem. Geol. 104, 189–202.

Ferraro, J.R., Nakamoto, K., Brown, C.W., 2003. Introductory Raman Spectroscopy. Academic Press, San Diego, CA.

Goldfarb, M.S., Converse, D.R., Holland, H.D., Edmond, J.M., 1983. The genesis of hot spring deposits on the East Pacific Rise, 21°N. In: Ohmoto, H., Skinner, B.J. (Eds.), Economic Geology Monograph, pp. 184–197.

Greinert, J., Bollwerk, S.M., Derkachev, A., Bohrmann, G., Suess, E., 2002. Massive barite deposits and carbonate mineralization in the Derugin Basin, Sea of Okhotsk: precipitation processes at cold seep sites. Earth Planet. Sci. Lett. 203, 165–180.

Hannington, M.D., Scott, S.D., 1988. Mineralogy and geochemistry of a hydrothermal silica–sulfide–sulfate spire in the caldera of Axial Seamount, Juan de Fuca. Can. Mineral. 26 (3), 603–625.

Hannington, M.D., de Ronde, C.E., Petersen, S., 2005. Sea-floor tectonics and submarine hydrothermal systems. In: Hedenquist, J.W., Thompson, J.F.H., Goldfarb, R.J., Richards, J.P. (Eds.), Economic Geology 100th Anniversary Volume. Society of Economic Geologists, Littleton, Colorado, pp. 111–141.

Harvey, P.D., Butler, I.S., 1986. Raman spectra of orthorhombic sulfur at 40 K. J. Raman Spectrosc. 17, 329–334.

Haskin, L.A., et al., 1997. Raman spectroscopy for mineral identification and quantification for in situ planetary surface analysis: a point count method. J. Geophys. Res. 102 (E8), 19,293–19,306.

Haymon, R.M., 1983. Growth history of hydrothermal black smoker chimneys. Nature 301, 694–698.

Haymon, R.M., Kastner, M., 1981. Hot spring deposits on the East Pacific Rise at 21°N: preliminary description of mineralogy and genesis. Earth Planet. Sci. Lett. 53, 363–381.

Hessler, R.R., Kaharl, V.A., 1995. The deep-sea hydrothermal vent community. In: Humphris, S.E., Zierenberg, R.A., Mullineaux, L.S., Thomson, R.E. (Eds.), Seafloor Hydrothermal Systems: Physical, Chemical, Biological, and Geological Interactions. AGU, Washington, DC.

Hester, K.C., et al., 2007. Gas hydrate measurements at Hydrate Ridge using Raman spectroscopy. Geochim. Cosmochim. Acta 71, 2947–2959.

Hester, K.C., White, S.N., Peltzer, E.T., Brewer, P.G., Sloan, E.D., 2006. Raman spectroscopic measurements of synthetic gas hydrates in the ocean. Mar. Chem. 98, 304–314.

Kharbish, S., 2007. A Raman spectroscopic investigation of Fe-rich sphalerite: effect of Fe-substitution. Phys. Chem. Miner. 34, 551–558.

Kroumova, E., et al., 2003. Bilbao crystallographic server: useful databases and tools for phase-transition studies. Phase Transit. Multinatl. J. 76, 155–170.

Landsberg, G., Mandelstam, L., 1928. Eine neue Erscheinung bei der Lichtzerstreuung in Krystallen. Naturwissenschaften 16, 557–558.

Leonard, D.A., Caputo, B., Hoge, F.E., 1979. Remote sensing of subsurface water temperature by Raman scattering. Appl. Opt. 18 (11), 1732–1745.

Lonsdale, P., 1979. A deep-sea hydrothermal site on a strike–slip fault. Nature 281, 531–534.

Luff, R., Wallmann, K., Aloisi, G., 2004. Numerical modeling of carbonate crust formation at cold vent sites: significance for fluid and methane budgets and chemosynthetic biological communities. Earth Planet. Sci. Lett. 221, 337–353.

Lutz, H.D., Müller, B., 1991. Lattice vibration spectra. LXVIII. Single-crystal Raman spectra of marcasite-type iron chalcogenides and pnictides, FeX_2 (X=S, Se, Te; P, As, Sb). Phys. Chem. Miner. 18, 265–268.

Mao, H., Hemley, R.J., Chao, E.C.T., 1987. The application of micro-Raman spectroscopy to analysis and identification of minerals in thin section. Scanning Microsc. 1 (2), 495–501.

Marfunin, A.S., 1979. Spectroscopy, Luminescence and Radiation Centers in Minerals. Springer-Verlag, Berlin. 352 pp.

Matousek, P., Towrie, M., Stanley, A., Parker, A.W., 1999. Efficient rejection of fluorescence from Raman spectra using picosecond Kerr gating. Appl. Spectrosc. 53 (12), 1485–1489.

Matousek, P., et al., 2001. Fluorescence suppression in resonance Raman spectroscopy using a high-performance picosecond Kerr gate. J. Raman Spectrosc. 32, 983–988.

Mernagh, T.P., Trudu, A.G., 1993. A laser Raman microprobe study of some geologically important sulphide minerals. Chem. Geol. 103, 113–127.

Naehr, T.H., Stakes, D.S., Moores, W.S., 2000. Mass wasting, ephemeral fluid flow, and barite deposition on the California continental margin. Geology 28 (4), 315–318.

Nakamoto, K., 1997. Infrared and Raman Spectra of Inorganic and Coordination Compounds: Part A. John Wiley & Sons, Inc., New York, NY. 387 pp.

Nakamura, K., et al., 2006. Liquid and emulsified sulfur in submarine solfatara fields of two Northern Mariana arc volcanoes. Fall Meet. Suppls., Abstract V23B–0608. Eos Trans. AGU, vol. 87(52).

Nasdala, L., Smith, D.C., Kaindl, R., Ziemann, M.A., 2004. Raman spectroscopy: analytical perspectives in mineralogical research. In: Beran, A., Libowitzky, E. (Eds.), EMU Notes in Mineralogy: Spectroscopic Methods in Mineralogy. European Mineralogical Union, pp. 281–343.

Nichols, E.L., Howes, H.L., Wilber, D.T., 1918. The photoluminescence and kathodo-luminescence of calcite. Phys. Rev. 12 (5), 351–367.

Ozin, G.A., 1969. The single-crystal Raman spectrum of rhombic sulphur. J. Chem. Soc., A 116–118.

Pasteris, J.D., 1998. The laser Raman microprobe as a tool for the economic geologist. In: McKibben, M.A., Shanks, W.C., Ridley, W.I. (Eds.), Applications of Microanalytical Techniques to Understanding Mineralizing Processes. Society of Economic Geologists, Littleton, CO, pp. 233–250.

Pasteris, J.D., Freeman, J.J., Goffredi, S.K., Buck, K.R., 2001. Raman spectroscopic and laser scanning confocal microscopic analysis of sulfur in living sulfur-precipitating marine bacteria. Chem. Geol. 180, 3–18.

Pasteris, J.D., et al., 2004. Raman spectroscopy in the deep ocean: successes and challenges. Appl. Spectrosc. 58 (7), 195A–208A.

Prien, R., 2007. The future of chemical in situ sensors. Mar. Chem. 107, 422–432.

Raman, C.V., Krishnan, K.S., 1928. A new type of secondary radiation. Nature 121, 501–502.

Rona, P.A., Klinkhammer, G., Nelsen, T.A., Trefry, J.H., Elderfield, H., 1986. Black smokers, massive sulphides and vent biota at the Mid-Atlantic Ridge. Nature 321, 33–37.

Sibuet, M., Olu, K., 1998. Biogeography, biodiversity and fluid dependence of deep-sea cold-seep communities at active and passive margins. Deep-Sea Res. II 45 (1), 517–567.

Smith, D.C., Carabatos-Nédelec, 2001. Raman spectroscopy applied to crystals: phenomena and principles, concepts and conventions. In: Lewis, I.R., Edwards, H.G.M. (Eds.), Handbook of Raman Spectroscopy. Practical Spectroscopy. Marcel Dekker, Inc., New York, pp. 349–422.

Smith, G.D., Clark, R.J.H., 2002. The role of H_2S in pigment blackening. J. Cult. Herit. 3, 101–105.

Stopar, J.D., et al., 2005. Raman efficiencies of natural rocks and minerals: performance of a remote Raman system for planetary exploration at a distance of 10 meters. Spectrochim. Acta, A 61, 2315–2323.

Taylor, C.D., Wirsen, C.O., 1997. Microbiology and ecology of filamentous sulfur formation. Science 277, 1483–1485.

Tivey, M.K., 1995. Modeling chimney growth and associated fluid flow at seafloor hydrothermal vent sites. In: Humphris, S.E., Zierenberg, R.A., Mullineaux, L.S., Thomson, R.E. (Eds.), Seafloor Hydrothermal Systems: Physical, Chemical, Biological, and Geological Interactions. AGU, Washington, D. C.

Tivey, M.K., 2007. Generation of seafloor hydrothermal vent fluids and associated mineral deposits. Oceanography 20 (1), 50–65.

Tivey, M.K., Delaney, J.R., 1986. Growth of large sulfide structures on the Endeavour Segment of the Juan de Fuca Ridge. Earth Planet. Sci. Lett. 77, 303–317.

Tivey, M.K., McDuff, R.E., 1990. Mineral precipitation in the walls of black smoker chimneys: a quantitative model of transport and chemical reactions. J. Geophys. Res. 95 (B8), 12,617–12,637.

Tivey, M.K., et al., 2005. Characterization of six vent fields within the Lau Basin. Fall Meet. Suppl., Abstract T31A-0477. Eos Trans. AGU, vol. 86(52).

Torres, M.E., Bohrmann, G., Dube, T.E., 2003. Formation of modern and Paleozoic stratiform barite at cold methane seeps on continental margins. Geology 31 (10), 897–900.

Turcotte, S.B., et al., 1993. Application of Raman spectroscopy to metal-sulfide surface analysis. Appl. Opt. 32 (6), 935–938.

Urmos, J., Sharma, S.K., Mackenzie, F.T., 1991. Characterization of some biogenic carbonates with Raman spectroscopy. Am. Mineral. 76, 641–646.

Ushioda, S., 1972. Raman scattering from phonons in iron pyrite (FeS2). Solid State Commun. 10, 307–310.

Varney, M.S. (Ed.), 2000. Chemical Sensors in Oceanography. Gordon & Breach, Netherlands. 333 pp.

Wang, A., Haskin, L.A., Cortez, E., 1998. Prototype Raman spectroscopic sensor for in situ mineral characterization on planetary surfaces. Appl. Spectrosc. 52 (4), 477–487.

Wang, A., et al., 2003. Development of the Mars microbeam Raman spectrometer (MMRS). J. Geophys. Res. 108 (E1) (10.1029/2002EJ001902).

Wang, A., Kuebler, K., Jolliff, B.L., Haskin, L.A., 2004. Mineralogy of a Martian meteorite as determined by Raman spectroscopy. J. Raman Spectrosc. 35, 504–514.

White, S.N., et al., 2005. Development and deployment of a precision underwater positioning system for in situ laser Raman spectroscopy in the deep ocean. Deep-Sea Res. I 52, 2376–2389.

White, S.N., Brewer, P.G., Peltzer, E.T., 2006a. Determination of gas bubble fractionation rates in the deep ocean by laser Raman spectroscopy. Mar. Chem. 99, 12–23.

White, S.N., Dunk, R.M., Brewer, P.G., Peltzer, E.T., Freeman, J.J., 2006b. In situ Raman analyses of deep-sea hydrothermal and cold seep systems (Gorda Ridge & Hydrate Ridge). Geochem. Geophys. Geosyst. 7 (5), Q05023. doi:10.1029/2005GC001204.

Wiens, R.C., Sharma, S.K., Thompson, J., Misra, A., Lucey, P.G., 2005. Joint analyses by laser-induced breakdown spectroscopy (LIBS) and Raman spectroscopy at stand-off distances. Spectrochim. Acta, A 61, 2324–2334.

Williams, T.L., Collette, T.W., 2001. Environmental applications of Raman spectroscopy to aqueous systems. In: Lewis, I.R., Edwards, H.G.M. (Eds.), Handbook of Raman Spectroscopy. Practical Spectroscopy. Marcel Dekker, Inc., New York, pp. 683–731.

Wopenka, B., Pasteris, J.D., 1987. Raman intensities and detection limits of geochemically relevant gas mixtures for a laser Raman microprobe. Anal. Chem. 59, 2165–2170.